A Functional Subgrid Drift Velocity Model for Filtered Drag Prediction in Dense Fluidized Bed

Jean-François Parmentier and Olivier Simonin
Université de Toulouse; INPT, UPS; Institut de Mécanique des Fluides de Toulouse; F-31400 Toulouse, France, and
CNRS; IMFT, UMR 5502; Allée Camille Soula, 31400 Toulouse, France

Olivier Delsart
TOTAL CReG, BP 27, F-76700 Harfleur, France

Due to computational time limitations, fully resolved simulations using the two-fluid model of the flow inside industrial-scale fluidized beds are unaffordable. The filtered approach is used to account for the effect of small unresolved scales on the large resolved scales computed with "coarse" realistic meshes. Using a fully resolved simulation, we highlight the need to account for a subgrid drift velocity to obtain the correct bed expansion when using coarse meshes. This velocity, defined as the difference between the filtered gas velocity seen by the particle phase and the resolved filtered gas velocity, modify the effective relative velocity appearing in the drag law. We close it as a correction of the resolved relative velocity depending on the filtered particle concentration and the filter size. A dynamic procedure is used to adjust a tuning parameter. Bed expansion obtained with a posteriori test on coarse-grid simulations matches well to fully resolved simulations. © 2011 American Institute of Chemical Engineers AIChE J, 58: 1084–1098, 2012
Keywords: computational fluid dynamics (CFD), fluid mechanics, fluidization, mathematical modeling, multiphase flow

Introduction

This study is concerned with the problem of the prediction of gas-particle flows in the specific domain of dense fluidized beds. Fluidization is the operation by which solid particles are transformed into a fluid-like state through suspension in a gas or liquid. When a fluid is passed upward through a bed of particles at a sufficient flow rate, particles become agitated and large instabilities with bubbling and channelling of gas are observed. When the flow rate is large enough to transport particles, the fluidized bed is said to be circulating. Bubbling fluidized beds and circulating fluidized beds are widely used in several industrial applications.[1] Due to large instabilities, flow is difficult to describe and predict. Computational fluid dynamics (CFD) offers a powerful tool to analyze the multiscale nature of the flow inside large scale processes.[2,3]

Among the various CFD methods available, the two-fluid method, also called the Eulerian approach, is the most suitable for engineering applications.[2] A continuum description is employed for both the gas phase and the solid phase. Closures are needed for both the drag force and the stress tensor of the particle phase (particle pressure and viscosity). An adapted kinetic theory of granular flows is employed to

provide closures for the particle stress tensor. This approach has been applied with success to group B particles.[4–8] However, the application of this method to bubbling and turbulent fluidized beds of fine Geldart A particles leads to severe overestimation of the bed expansion.[9–15] The drag law is a key parameter in the prediction of the bed expansion and several closures can be found in the literature.[16–21] Nevertheless, all the closures lead to the same order of overestimation.

The origin of the problem is still under discussion. McKeen and Pugsley[13] argued that this difference could be related to the presence of inter-particle forces (IPF) such as Van deer Waals forces. IPF lead to the formation of clusters and consequently to a modification of the effective particle size in the drag law. By fitting their numerical results to their experimental data, the authors found an effective particle agglomerate diameter of around 150 μm. However, the bed expansion predicted by their numerical simulation decreases as the mesh size decreases. As they do not achieve mesh convergence, their analysis is questionable.

As shown by Parmentier et al.[22] in case of a very coarse grid, field of particle volume fraction predicted by the numerical simulation of Geldart A particles is nearly homogeneous. The corresponding bed height is of the order of the height found by assuming an homogeneous equilibrium in the momentum transport equations of particle and gas phase. When the ratio between the superficial gas velocity and the terminal velocity of particles tends to one, the homogeneous bed expansion goes to infinity, while the real flow leads to the formation of bubbles and a finite bed expansion. Hence, numerical simulations lead to a major overestimation of the bed expansion. This supports the idea that the overestimation is mainly due to the effect of unresolved structures on the resolved flow. Moreover, Wang et al.[23] performed highly resolved three-dimensional simulations of a bubbling fluidized bed at moderate superficial gas velocity. By comparing their results to those obtained using Lagrangian simulations, they concluded that the standard two-fluid model with the standard Gidaspow[24] drag law does not lead to an overestimation of the bed expansion when sufficiently fine meshes are used.

The influence of the mesh size on the macroscopic behaviour is also found in circulating fluidized bed.[25–29] Agrawal et al.[25] and Igci et al.[28] have shown that if small structures of the flow are not completely solved, the drag force is overestimated. As a consequence, the mesh size is a key parameter in the numerical simulation of fluidized beds when using the two-fluid model.

Various methods are proposed in the literature to modify the drag term to obtain the correct bed expansion (for a state-of-the art review, we refer to Wang[14]). McKeen and Pugsley[13] suggested to use a scale factor between 0.2 and 0.3 for the commonly used gas-solid drag laws. With this factor, their numerical simulations fit their experimental results well. Following the same analysis, Hosseini et al.[11] used a scale factor of 0.1 to fit their own experiments. Gao et al.[10] used an effective mean diameter of 300 μm for the dense phase of their turbulent fluidized bed, corresponding to a scale factor of 0.04. None of the authors propose a generic law to estimate this scale factor.

Andrews IV et al.[26] to use an ad hoc effective drag coefficient to perform simulation of a large-scale circulating fluidized bed on a coarse grid. Their effective drag coefficient is measured using the highly resolved simulations of periodic flows obtained by Agrawal et al.[25] and depends on the particle volume fraction. Following the same approach, Igci et al.[28] propose an effective drag coefficient that depends on the size of the filter used, i.e., the size of the grid used in numerical simulations.

Recently, the EMMS method has been applied to the prediction of the hydrodynamics inside a bubbling fluidized bed.[30] The EMMS method, originally developed by Li and Kwauk[31] to predict steady flows inside circulating fluidized beds, assumes that particles move in the form of clusters through a dilute phase composed by the surrounding gas and a few randomly distributed particles. The EMMS method was integrated into the Eulerian formalism in the form of a subgrid drag correction.[32] The last revised EMMS model can be found in Wang et al.[33] Clusters are described by 10 parameters that are calculated by balance laws and an energy minimization condition. While a good agreement is found between simulation results of Wang and Liu[30] and experimental results, the description of the flow in the form of clusters is very questionable in a dense bubbling fluidized bed where bubbles move inside a dense phase composed of little gas and highly concentrated particles.

Finally, Wang et al.[34] show that a correction of the drag law is also needed when performing coarse grid simulations of industrial-scale bubbling fluidized beds with Geldart B particles. By assuming that the flow inside each computational cell is divided into a dense zone, where the relative velocity is given by a homogeneous expansion law,[35] and a dilute zone where no particles are present, the authors propose a simple modification of the drag law. Such a relationship between the gas velocity and the particle volume fraction is a very limiting parameter.

Starting from the filtered equations of the two-fluid model and using a highly resolved simulation of a bubbling fluidized bed of Geldart A particles, we will demonstrate that the overestimation of the filtered drag is linked to the existence of a subgrid drift velocity that should be taken into account. Then, we will suggest to close this subgrid drift velocity by assuming that its function is to reduce the effective relative velocity. Hence, it is expressed as a correction to the resolved relative velocity, depending on the filtered particle volume fraction and on the filter size. This model will be constructed using results of the highly resolved simulation. Moreover, a dynamic procedure will be used to adjust a tuning parameter. Finally, this model will be first tested a priori using the highly resolved simulation and then tested a posteriori on coarse-grid simulations.

Filtered Two-Fluid Model Equations

We start from the point that small structures are predicted by the two-fluid model equations and that these structures have a drastic influence on the bed expansion. Due to practical limitations, these structures cannot be resolved for simulations at the pilot or industrial scale. Hence, they need to be modeled. The filtered approach is a formalism that highlights terms that need to be closed when we do not wish to solve small structures. This idea has been applied in single-phase turbulent flow for many years,[36] but the application to gas-particle flows is very recent.[25,26,28,29]

Table 1. Table of Useful Symbols

Symbol	Name	Unit
α_k	Phase volume fraction	
$\overline{\alpha}_p$	Filtered particle volume fraction (Eq. 2)	
d_p	Particle diameter	μm
Δ_G	Cells size	m
$\overline{\Delta}$	Filter size	m
$\overline{\Delta}^*$	Dimensionless filter size (Eq. 29)	
$\|\mathbf{g}\|$	Norm of the gravity	m/s^2
L	Bed width	m
μ_g	Gas viscosity	Pa.s
P_g	Filtered gas pressure	Pa
$\overline{P}_g$	Filtered gas pressure (Eq. 1)	Pa
ρ_k	Phase density	Kg/m^3
τ_p	Particle relaxation time	s
$\widetilde{\tau}_g$	Filtered particle relaxation time (Eq. 7)	s
τ_p^{St}	Stokes drag time of an isolated particle	s
U_f	Superficial gas velocity	m/s
$U_{k,i}$	Phase velocity	m/s
$\widetilde{U}_{g,i}$	Filtered gas velocity (Eq. 4)	m/s
$\widetilde{U}_{g@p,i}$	Filtered gas velocity seen by the particle phase (Eq. 17)	m/s
$\widetilde{U}_{p,i}$	Filtered particle velocity(Eq. 3)	m/s
$\widetilde{V}_{d,i}$	Subgrid drift velocity (Eq. 19)	m/s
$V_{r,i}$	Relative velocity ($= U_{p,i} - U_{g,i}$)	m/s
$\widetilde{W}_{r,i}$	Resolved relative velocity ($\widetilde{U}_{p,i} - \widetilde{U}_{g,i}$)	m/s

Subscript k stands for the phase: $k = g$ for the gas and $k = p$ for the particles. Subscript i stands for the direction of the space.

The idea is to split all physical variables into a resolved part and an unresolved part. The resolved part of a variable is the spatially filtered variable, which contains only large-scale structures that can be resolved on a coarse-grid. The unresolved part contains the small scales that cannot be solved on a coarse grid. The balance laws of the filtered variables are found by filtering the balance laws of the two-fluid model. While we have chosen a particular set of constitutive relations for the two-fluid model, detailed in Appendix, the approach can be applied to other relations.

Let us define $\overline{f}(\mathbf{x},t)$ as the filtered part—or the resolved part—of a space-time variable $f(\mathbf{x}, t)$ as:

$$\overline{f}(\mathbf{x},t) = \int \int \int G(\mathbf{x} - \mathbf{y}) f(\mathbf{y},t) \, \mathbf{dy} \qquad (1)$$

where G is a weight function that satisfies $\int \int\int G(\mathbf{y})\mathbf{dy} = 1$. Several choices can be made for the weight function. By choosing how rapidly $G(\mathbf{y})$ decays when y increases, one can change how much the small structures will be taken into account in the resolved part. Hence, the filtered particle volume fraction $\overline{\alpha}_p$ is defined according to Eq. 1:

$$\overline{\alpha}_p(\mathbf{x},t) = \int \int \int G(\mathbf{x} - \mathbf{y}) \, \alpha_p(\mathbf{y},t) \, \mathbf{dy} \qquad (2)$$

The gas phase pressure, $\overline{P}_g(\mathbf{x},t)$, is similarly defined. Filtered phase velocities are defined by:

$$\widetilde{U}_{p,i} = \overline{\alpha_p U_{p,i}} / \overline{\alpha}_p \qquad (3)$$

$$\widetilde{U}_{g,i} = \overline{\alpha_g U_{g,i}} / \overline{\alpha}_g \qquad (4)$$

where the subscript i stands for the direction $(x, y,$ or $z)$. The filtered particle agitation is defined by $\widetilde{q}_p^2 = \overline{\alpha_p q_p^2} / \overline{\alpha}_p$.

The balance laws for the filtered variables are obtained by filtering the balance laws of the two-fluid model, leading, for the mass transport equations, to:

$$\frac{\partial}{\partial t} (\rho_k \, \overline{\alpha}_k) + \frac{\partial}{\partial x_j} (\rho_k \, \overline{\alpha}_k \widetilde{U}_{k,j}) = 0 \qquad (5)$$

where the subscript $k = p$ for the particle phase and $k = g$ for the gas phase (Table 1). A direct consequence of the definition of the filtered phase velocities Eqs. 3 and 4 is that Eqs. 5 are formally similar to those of the two-fluid model. Filtering the momentum transport equation of the particle phase leads to:

$$\rho_p \, \overline{\alpha}_p \, \frac{D\widetilde{U}_{p,i}}{Dt} = \rho_p \, \overline{\alpha}_p \, g_i$$
$$- \overline{\alpha}_p \, \frac{\partial \overline{P}_g}{\partial x_i} - \Phi_{P,i}$$
$$- \rho_p \, \frac{\overline{\alpha}_p \widetilde{W}_{r,i}}{\widetilde{\tau}_p} - \Phi_{D,i}$$
$$- \frac{\partial}{\partial x_j} \overline{\Sigma}_{p,ij} - \frac{\partial}{\partial x_j} (\rho_p \, \overline{\alpha}_p \sigma_{p,ij}) \qquad (6)$$

where $\widetilde{W}_{r,i} = \widetilde{U}_{p,i} - \widetilde{U}_{g,i}$ is the resolved relative velocity. The particle relaxation time τ_p is given by the Wen and Yu[21] drag law (Eq. A15), and $\widetilde{\tau}_p$ is defined similarly using the resolved part of the variables:

$$\frac{1}{\widetilde{\tau}_p} = \frac{1}{\tau_p^{St}} \left(1 + 0.15 \widetilde{R}_e^{0.687}\right) \overline{\alpha}_g^{-2.7} \qquad (7)$$

$\widetilde{R}_e = \overline{\alpha}_g \|\widetilde{\mathbf{U}}_\mathbf{p} - \widetilde{\mathbf{U}}_\mathbf{g}\| d_p / \nu_g$ and $\tau_p^{St} = \rho_p d_p^2/(18\mu_g)$ the Stokes drag time of an isolated particle. Four terms have to be closed: the filtered particle stress, $\overline{\Sigma}_{p,ij}$, a Reynolds stress-like contribution coming from the particle phase velocity fluctuations, $\sigma_{p,ij}$ defined by:

$$\overline{\alpha}_p \sigma_{p,ij} = \overline{\alpha_p U_{p,i} U_{p,j}} - \overline{\alpha}_p \widetilde{U}_{p,i} \widetilde{U}_{p,j} \qquad (8)$$

and $\Phi_{P,i}$ and $\Phi_{D,i}$, defined by:

$$\Phi_{P,i} = \overline{\alpha_p \frac{\partial P_g}{\partial x_i}} - \overline{\alpha}_p \frac{\partial \overline{P}_g}{\partial x_i} \qquad (9)$$

$$\Phi_{D,i} = \rho_p \overline{\left(\frac{\alpha_p V_{r,i}}{\tau_p}\right)} - \rho_p \frac{\overline{\alpha}_p \widetilde{W}_{r,i}}{\widetilde{\tau}_p} \qquad (10)$$

where $V_{r,i} = U_{p,i} - U_{g,i}$ is the relative velocity. The balance law for the filtered gas velocity can be obtained by filtering the gas phase momentum equation, leading to another unknown term, $\sigma_{g,ij}$, defined by:

$$\overline{\alpha}_g \sigma_{g,ij} = \overline{\alpha_g U_{g,i} U_{g,j}} - \overline{\alpha}_g \widetilde{U}_{g,i} \widetilde{U}_{g,j} \qquad (11)$$

In the following, the balance law of the filtered particle agitation is assumed to be similar to Eq. A11 when using the filtered variables. This amounts to say that unresolved terms appearing in this equation are assumed to have a negligible effect on the bed expansion.

Case Description

To study the effect of unresolved structures on the resolved flow in dense bubbling fluidized beds, a simple bidimensional
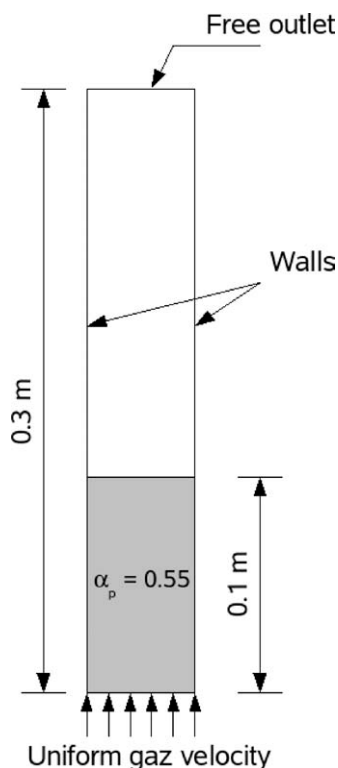
Figure 1. Geometry, initial, and boundary conditions used in the 2D simulation of the bubbling fluidized bed.

test case is used as a reference. The geometry is given in Figure 1. This case will be numerically simulated using different meshes. Constitutive relations derived by Balzer et al.[4] (see Appendix), with the Wen and Yu[21] drag law, are solved using NEPTUNE_CFD, an unstructured parallelized multiphase flow software.[37]

Gas and solid properties are summarized in Table 2. The ratio between the superficial gas velocity and the terminal velocity of an isolated particle is around 0.9. Particles and gas properties are typical for FCC particles fluidized by ambient air. Boundary conditions are given in Figure 1. Gas no-slip and particle free slip (with zero kinetic energy flux) boundary conditions are applied on the walls.

The geometry is meshed using uniform square cells. Cells size, Δ_G, goes from 2 mm for the coarsest grid, to 100 μm for the finest grid. Figure 2 shows instantaneous snapshots of the particle volume fraction obtained with the meshes. Time-averaged profiles are shown in Figure 3. It is readily apparent that finer structures are resolved as the spatial grid is refined, leading to a decrease of the bed expansion. Time-averaged quanti-

Table 2. Physical Parameters

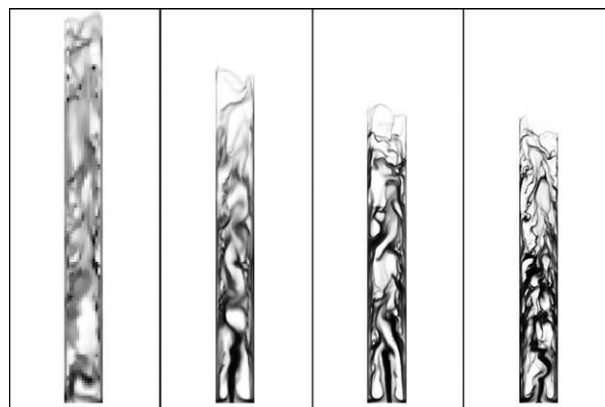|	
Bed width L	3 cm
Particle diameter d_p	75 μm
Particle density ρ_p	1500 kg/m^3
Restitution coefficient e_c	0.95
Gas density ρ_g	1.186 kg/m^3
Gas viscosity μ_g	$1.8 \ 10^{-5}$ Pa.s
Superficial gas velocity U_f	0.2 m/s

Figure 2. Instantaneous particle volume fraction field in the fluidized bed for different grid mesh sizes.

From left to right, $\Delta_G = 2$ mm, 1 mm, 500 μm, and 100 μm. White: $\alpha_p = 0$, black: $\alpha_p = 0.64$.

ties become mesh-size independent for mesh sizes smaller than 500 μm. The probability density function of the particle volume fraction is very sensitive to the grid resolution, as shown in Figure 4. It shows two high peaks, close to zero and 60%, when the finest mesh is used. Such peaks are not predicted for a mesh size greater than 500 μm. The numerical results obtained on the finest mesh will be used to provide closures for unknown terms appearing in Eq. 6.

A Priori Analysis Description

As the mesh convergence is reached when $\Delta_G = 100$ μm, the simulation is said to be fully resolved. Results are assumed to be a good discretization of the continuous solution of the two-fluid model. The mesh size will be noted Δ_D in the following, in reference to single-phase flow simulations, where such grid-size independent results are called "Direct Numerical Simulation." Hence, we get $\Delta_D = 100$ μm. These results are used to provide closures for the unknown terms appearing in Eq. 6 in the following way: for each snapshot of the flow field, the filtered quantities are calculated at each cell of the mesh, using for G a discrete version of the continuous box filter:

$$G(\mathbf{u}) = \begin{cases} 1/\Delta_B^2 & \text{if } max(u_x, u_z) < \Delta_B/2 \\ 0 & \text{otherwise} \end{cases} \quad (12)$$

Hence the instantaneous field of the filtered particle volume fraction, the filtered velocities, and so forth, are known for any value of Δ_B. The operation is repeated for typically 10 snapshots. As the mesh is composed of 900,000 cells, we get 9,000,000 of values for each filtered quantity and each value of Δ_B. All these filtered values are considered as statistically equivalent and are used to perform various averaging operations.

Subgrid Drift Velocity

Budget analysis

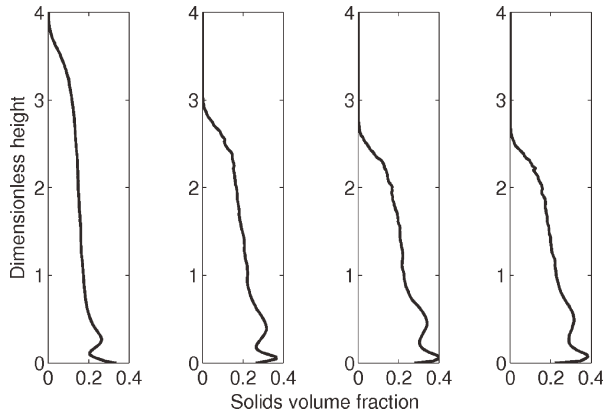The database described in the previous section is used to quantify the contribution of each term appearing in the

Figure 3. Vertical time-averaged profiles of the particle volume fraction, for x = 1.5 cm.

From left to right, $\Delta_G = 2$ mm, 1 mm, 500 μm, and 100 μm.

Figure 4. Probability density function of the particle volume fraction.

—: $\Delta_G = 100$ μm, ---: $\Delta_G = 1$ mm, ---: $\Delta_G = 2$ mm.

filtered momentum equation of the particle phase, Eq. 6. Let us define $\langle \overline{f} \rangle_{b,t}$ as the average of $\overline{f}$ over the entire bed and the time. Applying the $\langle . \rangle_{b,t}$ operation to Eq. 6 leads to:

$$
\begin{aligned}
0 = {} & \langle \rho_{\mathrm{p}} \, \overline{\alpha}_{\mathrm{p}} g_i \rangle_{b,t} \\
& - \langle \overline{\alpha}_{\mathrm{p}} \frac{\partial \overline{P}_{\mathrm{g}}}{\partial x_i} \rangle_{b,t} - \langle \Phi_{P,i} \rangle_{b,t} \\
& - \langle \rho_{\mathrm{p}} \frac{\overline{\alpha}_{\mathrm{p}} \widetilde{W}_{r,i}}{\widetilde{\tau}_{\mathrm{p}}} \rangle_{b,t} - \langle \Phi_{D,i} \rangle_{b,t}
\end{aligned}
\tag{13}
$$

Equation 13 simply states the global equilibrium between the filtered drag force, the filtered gravity and the filtered gas pressure gradient. The first term in the r.h.s. of Eq. 13 is the contribution of gravity. The second and the third are, respectively, the resolved and unresolved part of the buoyancy. The two last terms are the resolved and unresolved part of the drag force. The vertical components of these terms are plotted versus the Δ_B/Δ_D ratio in Figure 5. It is clear that, as the filter size increases, the resolved part of the drag force increases dramatically. In consequence, the unresolved part of the drag $\Phi_{D,i}$ decreases so that the average of the filtered drag remains constant. For this reason, when the filtered drag is estimated by its resolved part only—i.e., when $\Phi_{D,i}$ is neglected—the bed expansion is consequently overestimated. In contrast, the unresolved part of the buoyancy $\Phi_{P,i}$ remains negligible.

This analysis shows that the first-order term that needs to be modeled to predict the correct bed expansion of a bubbling fluidized bed is the unresolved part of the drag. Hence, we will focus on this term in the following. In circulating fluidized beds, some authors report that the contribution of the unresolved part of the buoyancy $\Phi_{P,i}$ is not negligible.[29,38,39] Effect of the Reynolds stress-like contribution $\sigma_{\mathrm{p},ij}$ and the filtered particle-stress $\overline{\Sigma}_{\mathrm{p},ij}$ were studied by Agrawal et al.[25] and Igci et al.[28] but are not the topic of this study as we are only interested on the prediction of the bed expansion.

Drift velocity

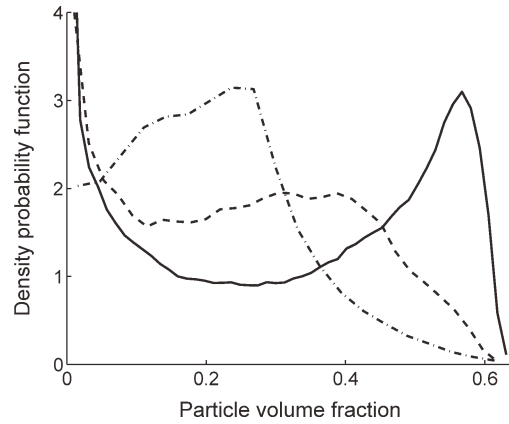To predict the correct fluidized bed expansion, we need to model the filtered drag force. Various authors have proposed a

closure law in the form of an effective drag coefficient[26–28,32] defined by:

$$
\overline{\left(\frac{\alpha_{\mathrm{p}} \rho_{\mathrm{p}}}{\tau_{\mathrm{p}}} V_{r,i} \right)} = \beta_e \, \widetilde{W}_{r,i}
\tag{14}
$$

This effective drag coefficient depends either on the filtered particle volume fraction[26,27] or on the filter size.[28] We will not follow this approach.

A correlative analysis using our database has shown that the filtered drag force can be approximated by:

$$
\overline{\left(\frac{\alpha_{\mathrm{p}} \rho_{\mathrm{p}}}{\tau_{\mathrm{p}}} V_{r,i} \right)} \simeq \frac{\rho_{\mathrm{p}}}{\widetilde{\tau}_{\mathrm{p}}} \, \overline{\alpha_{\mathrm{p}} V_{r,i}}
\tag{15}
$$

The r.h.s. of Eq. 15 is correlated with the l.h.s. to more than 99%, even for high values of Δ_B. It should be noted that the particle relaxation time depends both on the gas volume fraction and on the Reynolds number, which also depends on the relative velocity and on the gas volume
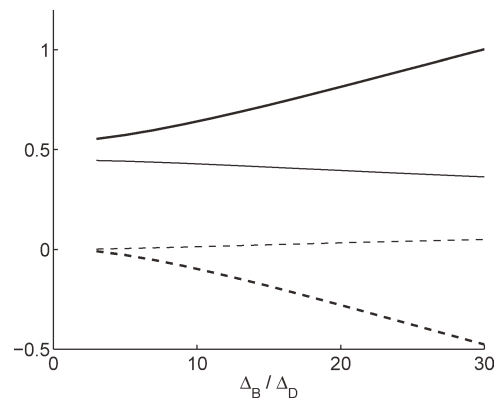

Figure 5. Budget analysis of Eq. 13 as a function of the ratio Δ_B/Δ_D.

—: resolved drag force, ---: unresolved drag force, —: resolved buoyancy, ---: unresolved buoyancy. All values are divided by the value of the gravity contribution.
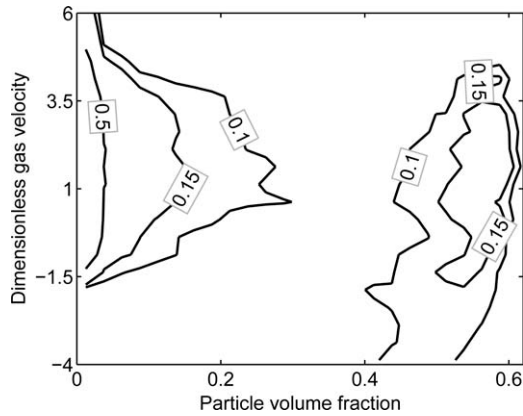
Figure 6. Iso values of the joint probability density function between the particle volume fraction and the gas velocity.

The gas velocity is made dimensionless using the superficial gas velocity.

fraction (Eq. 7). Equation 15 is an approximation and shows that the major challenge in predicting the filtered drag force is to produce a good model for the filtered relative velocity weighted by the particle volume fraction, $\overline{\alpha_p V_{r,i}}$. This last one is equal to:

$$\overline{\alpha_p V_{r,i}} = \overline{\alpha}_p \left(\widetilde{U}_{p,i} - \widetilde{U}_{g@p,i} \right) \qquad (16)$$

where:

$$\widetilde{U}_{g@p,i} = \overline{\alpha_p U_{g,i}} / \overline{\alpha}_p \qquad (17)$$

is the filtered gas velocity seen by the particle phase. Putting Eq. 16 in Eq. 15 leads the filtered drag force to:

$$\overline{\left(\frac{\alpha_p \rho_p}{\tau_p} V_{r,i} \right)} = \frac{\overline{\alpha}_p \rho_p}{\widetilde{\tau}_p} \left(\widetilde{W}_{r,i} - \widetilde{V}_{d,i} \right) \qquad (18)$$

where $\widetilde{V}_{d,i}$ is a subgrid drift velocity defined as the difference between the filtered gas velocity seen by the particle phase and the filtered gas velocity seen by the gas phase (defined Eq. 4):

$$\widetilde{V}_{d,i} = \widetilde{U}_{g@p,i} - \widetilde{U}_{g,i} \qquad (19)$$

$\widetilde{V}_{d,i}$ comes from the correlation between the particle volume fraction and the gas velocity as well as from spatial inhomogeneities inside the volume of filtering. The joint probability density function of the particle volume fraction and the gas velocity is shown in Figure 6. There is a strong dependence of the gas velocity on the particle volume fraction. As seen on Figure 7, the gas velocity is, on average, greater in dilute regions than in dense regions. Consequently the gas velocity seen by the gas phase will be greater, on average, than the gas velocity seen by the particle phase. Hence, the average drift velocity will be negative, reflecting the fact that the resolved part of the relative velocity overestimates the effective relative velocity.

A Taylor development shows that, for small filter size, the drift velocity can be written as (see Appendix):

$$\overline{\alpha}_p \overline{\alpha}_g \widetilde{V}_{d,i} = \frac{\overline{\Delta}^2}{12} \frac{\partial \alpha_p}{\partial x_j} \frac{\partial U_{g,i}}{\partial x_j} + O(\overline{\Delta}^4) \qquad (20)$$

with $\overline{\Delta}$ a characteristic length scale of the filter (for instance, when G is the continuous box filter, $\overline{\Delta} = \Delta_B$). Equation 20 shows that the drift velocity is proportional to the square of the filter size when the latter is small. Therefore, a model for the filtered drag should respect this square dependence for small filter size to be mathematically consistent.

Drag model description

General form

In previous sections, we have shown that the subgrid drift velocity defined by Eq. 19 needs to be modelled to predict the filtered drag force. The generic form to model it is given by:

$$\begin{aligned} \frac{\widetilde{V}_{d,i}}{\tau_p^{St}||\mathbf{g}||} = \mathcal{F}(\overline{\Delta}^*, \overline{\alpha}_p, \frac{\widetilde{W}_{r,j}}{\tau_p^{St}||\mathbf{g}||}, \\ \overline{\Delta}\frac{\partial \overline{\alpha}_p}{\partial x_j}, \overline{\Delta}\frac{\partial \widetilde{U}_{g,j}}{\partial x_k}, \overline{\Delta}\frac{\partial \widetilde{U}_{p,j}}{\partial x_k}, ..., \\ D_1, D_2, ..., D_n) \end{aligned} \qquad (21)$$

where $D_1, D_2, ..., D_n$ are dimensionless numbers that characterize the problem. The first dots refer to the combination of derivatives of variables. $\overline{\Delta}^*$ is a dimensionless parameter constructed with the filter size and the macroscopic fluidization parameters (bed width,...). As the first effect of the subgrid drift velocity is to reduce the effective relative velocity, we assume that it can be modelled by a simpler form:

$$\widetilde{V}_{d,i} = -g(\overline{\Delta}^*, \overline{\alpha}_p)K_{ij}\widetilde{W}_{r,j} \qquad (22)$$

where K_{ij} are constants and g is a function of the filtered particle volume fraction and a dimensionless filter size. Due to geometrical properties, it is assumed that $K_{xy} = K_{yx} = 0$. Only K_{xx} and K_{yy} have to be estimated and Eq. 22 can be written:
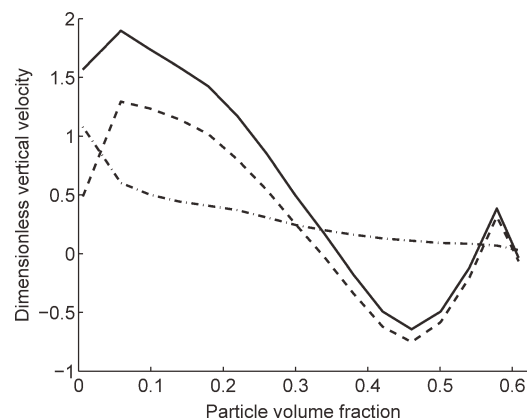

Figure 7. Average of vertical velocities conditioned by the particle volume fraction.

Velocity are made dimensionless using the superficial gas velocity. —: gas velocity, ---: particle velocity, -·-·: relative velocity.
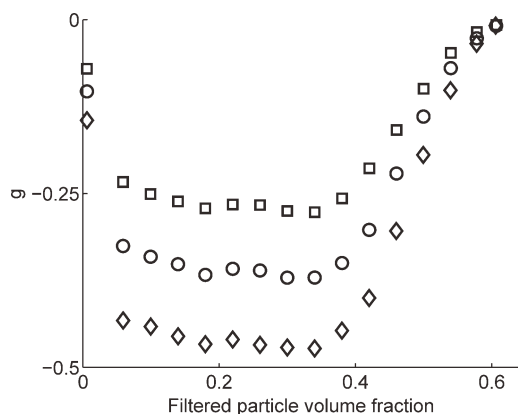
Figure 8. Measured values of *g* versus the filtered particle volume fraction $\overline{\alpha}_p$.

$\square$: $R = 11$, $\bigcirc$: $R = 15$, $\diamond$: $R = 21$.

$$\widetilde{V}_{d,\alpha} = \mathrm{g}(\overline{\Delta}^*, \overline{\alpha}_\mathrm{p}) K_{\alpha\alpha} \widetilde{W}_{r,\alpha} \qquad (23)$$

where the Greek subscript α is used to indicate that there is no implicit summation. The *g* function will be determined in the "Volume fraction and filter size dependence" section using the database provided by the fully resolved simulation and K_{ij} constants will be dynamically adjusted following a methodology adapted Germano et al.[40] and Lilly[41] described in the "Dynamic adjustment" section.

Volume fraction and filter size dependence

In this section, K_{yy} is assumed to be equal to one. The *g* function is determined using the database described in the "A Priori Analysis Description" section by:

$$\mathrm{g}(\overline{\Delta}^*, \overline{\alpha}_\mathrm{p}) = -\langle \widetilde{V}_{d,y} | \overline{\alpha}_\mathrm{p} \rangle_{b,t} / \langle \widetilde{W}_{r,y} | \overline{\alpha}_\mathrm{p} \rangle_{b,t} \qquad (24)$$

where $\langle A|B \rangle_{b,t}$ denotes the conditional average of A by B. *g* is plotted as a function of $\overline{\alpha}_p$ in Figure 8 for different values of $R = \Delta_B/\Delta_D$. As the shape of the function is nearly independent of R, *g* can be written as:
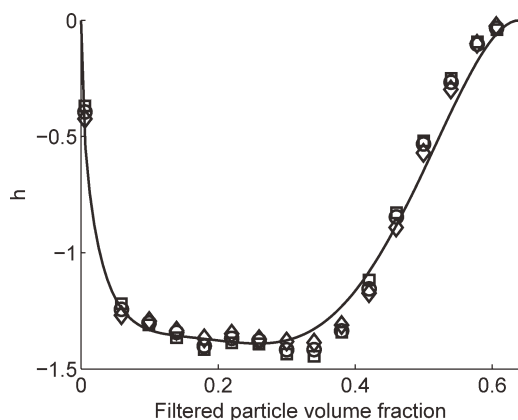

Figure 9. *h* versus the filtered particle volume fraction $\overline{\alpha}_p$. Symbols are obtained from the database.

$\square$: $R = 11$, $\bigcirc$: $R = 21$, $\diamond$: $R = 31$, —: Eq. 26.
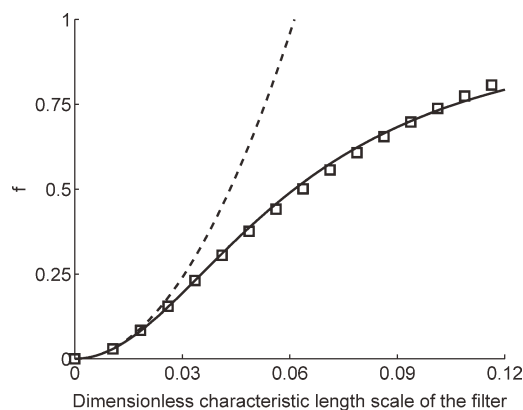

Figure 10. Evolution of *f* with respect to the dimensionless characteristic length scale of the filter, $\overline{\Delta}^*$.

$\square$: measured values, —: Eq. 28, ---: parabola.

$$\mathrm{g}(\overline{\Delta}^*, \overline{\alpha}_\mathrm{p}) \simeq f(\overline{\Delta}^*) \, h(\overline{\alpha}_\mathrm{p}) \qquad (25)$$

where $f(\overline{\Delta}*)$ and $h(\overline{\Delta}_p)$ are two independent functions. Measured values of *h* are represented in Figure 9 for different R. The following suggested form for *h* is obtained by fitting the measurements:

$$h(\overline{\alpha}_\mathrm{p}) = -\sqrt{u}(1 - u)^2 (1 - 1.88 \, u + 5.16 \, u^2) \qquad (26)$$

with $u = \overline{\alpha}_p/\alpha_m$ and $\alpha_m = 0.64$ representing the maximum loading. The suggested form for *h* was imposed to vanish when the filtered particle volume fraction was equal to either zero or the maximum loading. In these two cases, the particle volume fraction inside the filtering box is homogeneous. Hence, no correction to the filtered drag is needed. The maximum of the correction occurs for intermediate filtered particle volume fractions, reflecting the trend of the flow to lead to preferential particle volume fractions close to zero or to the maximum packing fraction, as shown in Figure 4.

The subgrid drift velocity dependence on the filter size is measured by:

$$f(\overline{\Delta}^*) = -\frac{\langle \overline{\alpha}_\mathrm{p} \widetilde{V}_{d,y} \rangle_{b,t}}{\langle \overline{\alpha}_\mathrm{p} h(\overline{\alpha}_\mathrm{p}) \widetilde{W}_{r,y} \rangle_{b,t}} \qquad (27)$$

f is plotted in Figure 10 and the following form is proposed:

$$f(\overline{\Delta}^*) = \frac{\overline{\Delta}^{*2}}{a^2 + \overline{\Delta}^{*2}} \qquad (28)$$

with $a \approx 6.13 \cdot 10^{-2}$ and $\overline{\Delta}*$ given by:

$$\overline{\Delta}^* = \frac{\overline{\Delta}/\tau_\mathrm{p}^{St}}{\sqrt{||\mathbf{g}||D_H}} \qquad (29)$$

where $D_\mathrm{H} = 2L$ the bed hydraulic diameter. Table 3 reports values of a obtained for a halved superficial gas velocity or a doubled bed width. The value is nearly case-independent. For small filter size, Eq. 28 leads to a parabola, which is consistent with the Taylor development given by Eq 20. For wide filter

Table 3. Measured Values of *a* for Different Cases

Case	*a*
Ref.	$6.13 \cdot 10^{-2}$
$U_f = 0.1$ m/s	$6.58 \cdot 10^{-2}$
$U_f = 0.1$ m/s and $L = 0.06$ m	$5.72 \cdot 10^{-2}$

Ref. is the case describe in the "A Priori Analysis Description" section. Other cases differ only as noted.

size, the filtered flow is homogeneous and the resolved part of the filtered drag reaches its maximal value. Consequently, *f* reaches a constant value, as shown in Figure 10.

Dynamic adjustment

Values of K_{xx} and K_{yy} depend on the simulated case. We propose to calculate them using a dynamic adjustment.[40] The main idea is that the model described in Eq. 23 is independent of the choice of the weight function *G* used to calculate filtered values. Therefore K_{ij} could be calculated by performing a second filter operation on the filtered quantities. This second filter, called the test filter, is applied during coarse grid simulations on resolved quantities.

Let us define $\hat{\bar{f}}$ by:

$$
\hat{\bar{f}}(\mathbf{x},t) = \frac{1}{5} \quad (\bar{f}(\mathbf{x},t)
$$
$$
+ \bar{f}(\mathbf{x} + \Delta_G \mathbf{e_x}, t) + \bar{f}(\mathbf{x} - \Delta_G \mathbf{e_x}, t) \qquad (30)
$$
$$
+ \bar{f}(\mathbf{x} + \Delta_G \mathbf{e_z}, t) + \bar{f}(\mathbf{x} - \Delta_G \mathbf{e_z}, t))
$$

where $\Delta_G \geq \Delta_B$. Equation 30 can be written in the form of a filtering operation on *f*. Its associated weight function has a characteristic length scale $\hat{\bar{\Delta}}$ linked to $\bar{\Delta}$ by:

$$
\hat{\bar{\Delta}}^2 = \bar{\Delta}^2 + \frac{24}{5}\Delta_G^2 \qquad (31)
$$

The filter associated with Eq. 30 is called the test filter.

Figures 11 and 12 show that calculating filtered quantities by Eq. 1 with the discrete box filter or the test filter leads to the same values for *f* and *h*. In consequence, one can write both:
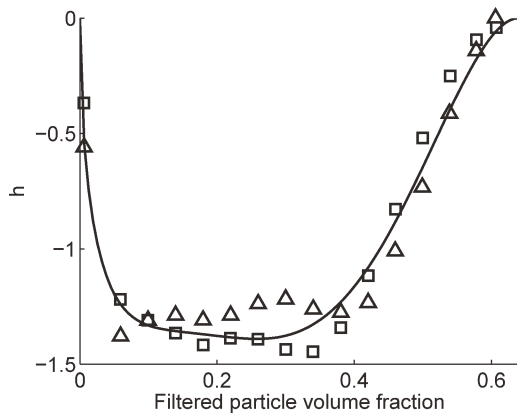

Figure 11. *h* as a function of the filtered particle volume fraction, $\bar{\alpha}_p$ or $\hat{\bar{\alpha}}_g$.

Symbols are obtained from the database. □: $R = 11$, discrete box filter, Δ: $R = 11$, test filter with $\Delta_G = \Delta_B$, —: Eq. 26.

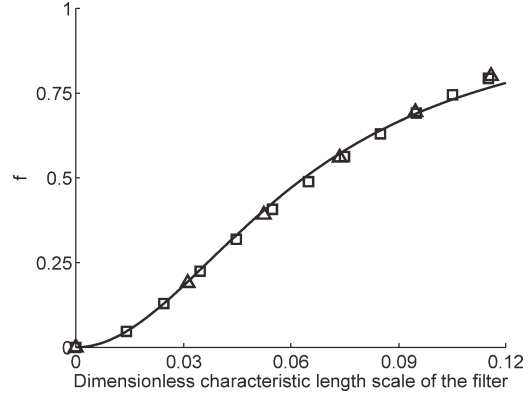**Figure 12. Evolution of *f* with respect to the dimensionless characteristic length scale of the filter, $\bar{\Delta}^*$ or $\hat{\bar{\Delta}}^*$.**

□: measured values with the box filter, Δ: measured values with the test filter, —: Eq. 28.

$$
\overline{\alpha_p V_{r,\alpha}} = \bar{\alpha}_p \tilde{W}_{r,\alpha}\left(1 + K_{\alpha\alpha}f(\bar{\Delta}^*)\,h(\bar{\alpha}_p)\right) \qquad (32)
$$

and

$$
\widehat{\overline{\alpha_p V_{r,\alpha}}} = \hat{\bar{\alpha}}_p \hat{\tilde{W}}_{r,\alpha}\left(1 + K_{\alpha\alpha}f(\hat{\bar{\Delta}}^*)\,h(\hat{\bar{\alpha}}_p)\right) \qquad (33)
$$

where $\hat{\tilde{W}}_{r,i}$ is defined by:

$$
\hat{\tilde{W}}_{r,i} = \hat{\tilde{U}}_{p,i} - \hat{\tilde{U}}_{g,i} \qquad (34)
$$

with $\hat{\tilde{U}}_{p,i} = \widehat{\overline{\alpha_g U_{p,i}}}/\hat{\bar{\alpha}}_g$ and $\hat{\tilde{U}}_{g,i} = \widehat{\overline{\alpha_g U_{g,i}}}/\hat{\bar{\alpha}}_g$. $\hat{\bar{\Delta}}^*$ is the dimensionless form of $\hat{\bar{\Delta}}$, defined using Eq. 29. By applying $\hat{(.)}$ operation on Eq. 32 then putting the result into Eq. 33, and assuming moreover that the scale of variation of $K_{\alpha\alpha}$ is much larger than the grid size:

$$
\left(K_{\alpha\alpha}\bar{\alpha}_p\widehat{h(\bar{\alpha}_p)}\tilde{W}_{r,\alpha}\right) \simeq K_{\alpha\alpha}\left(\bar{\alpha}_p\widehat{h(\bar{\alpha}_p)}\tilde{W}_{r,\alpha}\right) \qquad (35)
$$

$K_{\alpha\alpha}$ can be evaluated:

$$
K_{\alpha\alpha} \simeq -\frac{L_\alpha}{M_\alpha} \qquad (36)
$$

with L_α and M_α defined by:

$$
L_\alpha = \widehat{\bar{\alpha}_p\tilde{W}_{r,\alpha}} - \hat{\bar{\alpha}}_p\hat{\tilde{W}}_{r,\alpha} \qquad (37)
$$

$$
M_\alpha = f(\bar{\Delta}^*)(\widehat{\bar{\alpha}_p h(\bar{\alpha}_p)\tilde{W}_{r,\alpha}}) - f(\hat{\bar{\Delta}}^*)\hat{\bar{\alpha}}_p h(\hat{\bar{\alpha}}_p)\hat{\tilde{W}}_{r,\alpha} \qquad (38)
$$

Recapitulation

To summarize, we model the filtered drag force by:

$$
\overline{\left(\frac{\alpha_p\rho_p}{\tau_p}V_{r,\alpha}\right)} = \frac{\bar{\alpha}_p\rho_p}{\tilde{\tau}_p}\left(1 + f(\bar{\Delta}^*)h(\bar{\alpha}_p)K_{\alpha\alpha}\right)\tilde{W}_{r,\alpha} \qquad (39)
$$

where $f(\bar{\Delta}^*)$, $h(\bar{\alpha}_p)$, and $K_{\alpha\alpha}$ are evaluated using Eqs. 28, 26, and 36.

A Priori Validation

The highly resolved simulation results can be also used as a validation tool, to assess the validity of the model
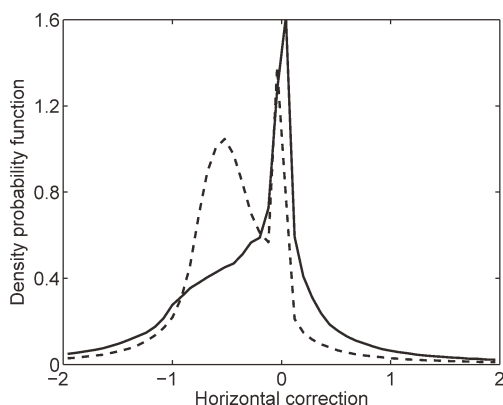
Figure 13. Probability density function of the horizontal correction of the drag, C_x, for $\Delta_B = 21\ \Delta_D$ and $\Delta_G = \Delta_B$, corresponding to $\overline{\Delta}^* \simeq 0.10$.

—: measured value, ---: model prediction.

developed. All filtered quantities are known, making comparison possible between the real filtered drag and the modelled one. The correction of the drag C_α in the α direction is defined by:

$$\frac{\overline{\alpha_p \rho_p}}{\tau_p} V_{r,\alpha} = \frac{\overline{\alpha_p \rho_p}}{\tilde{\tau}_p} \widetilde{W}_{r,\alpha}(1 + C_\alpha) \tag{40}$$

Putting Eq. 40 in Eq. 39 leads to the following model for C_α:

$$C_\alpha = f(\overline{\Delta}^*)\, h(\overline{\alpha}_p)\, K_{\alpha\alpha} \tag{41}$$

Figures 13 and 14 compare the probability density function of C_x and C_y measured in the bed with the prediction of Eq. 41, for $\Delta_B = 21\ \Delta_D$, corresponding to $\overline{\Delta}^* \simeq 0.10$, and $\Delta_G = \Delta_B$. Reasonable agreement is found. As seen in Figures 13 and 14, C_α could take values lower than -1. Such values result in a filtered drag force in the direction opposite to its resolved part (see Eq. 40).

Figure 15. Probability density function of the horizontal component of the drift velocity weighted by the filtered particle volume fraction, $\overline{\alpha}_p \widetilde{V}_{d,x}$, for $\Delta_B = 21\ \Delta_D$ ($\overline{\Delta}^* \simeq 0.10$), and $\Delta_G = \Delta_B$.

—: measured value, ---: model prediction.

Figures 15 and 16 compare the probability density function of $\overline{\alpha}_g \widetilde{V}_{d,x}$ and $\overline{\alpha}_g \widetilde{V}_{d,y}$ measured in the bed with the model prediction for $\overline{\Delta}^* \simeq 0.10$ and $\Delta_G = \Delta_B$. Both the probability density function of the horizontal and vertical components of the subgrid drift velocity are fairly well predicted. The probability density functions of the filtered drag, the resolved drag, and the filtered drag predicted by the model are shown in Figure 17. Fairly good agreement is again found.

Coarse-Grid Simulations

Two-dimensional coarse-grid simulations were performed using the theoretical model developed previously, and the results are compared with those obtained in highly resolved simulations. The theoretical developments rely on an abstract filter. A coarse-grid simulation is assumed to apply an implicit filter on calculated quantities, the length scale of which is proportional to the computational grid. As this
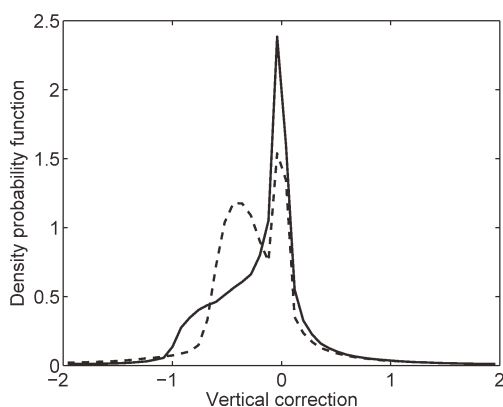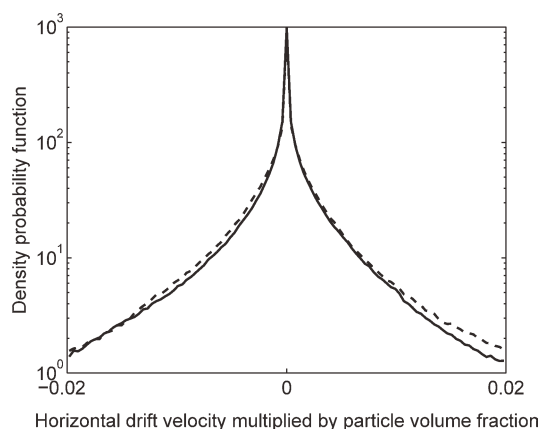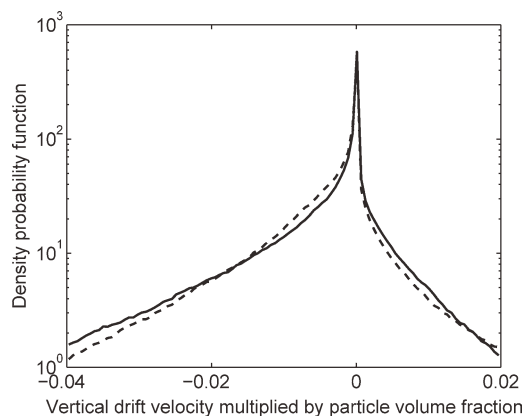

Figure 14. Probability density function of the vertical correction of the drag, C_y, for $\Delta_B = 21\ \Delta_D$ and $\Delta_G = \Delta_B$, corresponding to $\overline{\Delta}^* \simeq 0.10$.

—: measured value, ---: model prediction.

Figure 16. Probability density function of the vertical component of the drift velocity weighted by the filtered particle volume fraction, $\overline{\alpha}_p \widetilde{V}_{d,y}$, for $\Delta_B = 21\ \Delta_D$ ($\overline{\Delta}^* \simeq 0.10$), and $\Delta_G = \Delta_B$.

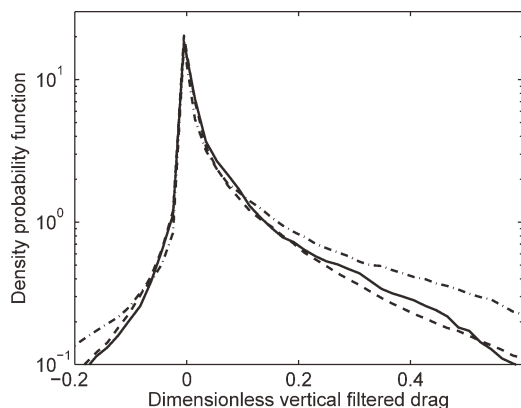—: measured value, ---: model prediction.

Figure 17. Probability density function of the dimensionless vertical component of the filtered drag for $\Delta_B = 21\,\Delta_D$ ($\overline{\Delta}^* \simeq 0.10$), and $\Delta_G = \Delta_B$.

—: measured value, ‑‑‑: model prediction, ‑‑‑‑: resolved drag.

implicit filter is unknown, the characteristic length scale $\overline{\Delta}$ is unknown. It is assumed that this length scale is related to the mesh size, Δ_G, by:

$$\overline{\Delta}^2 = 2\Delta_G^2 \tag{42}$$

The scale factor of 2 was determined empirically by adjusting the bed height obtained with the simulation of the test case on the 1 mm-mesh size (see the "coarse-grid simulation of the reference case" section).

For each time step and for each cell, K_{xx} and K_{yy} were calculated by applying the $(\hat{.})$ operation on the quantities given by the code. As shown in the a priori analysis, the corrections C_x and C_y could be less than -1. For numerical stability reasons, these values were set to -0.99. In the same way, predicted values of C_x and C_y greater than 0.99 were set to
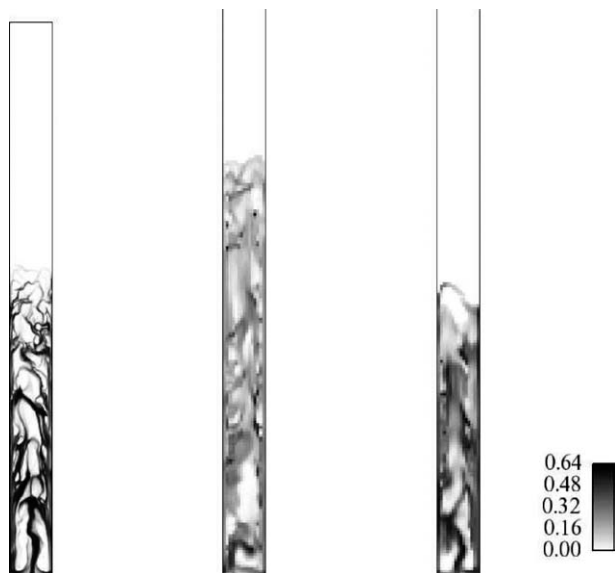

Figure 18. Instantaneous particle volume fraction field.

Fully resolved simulation (without any subgrid drag model) is at the left. Simulation on a 2 mm grid mesh size without and with the model are at the centre and at the right, respectively.
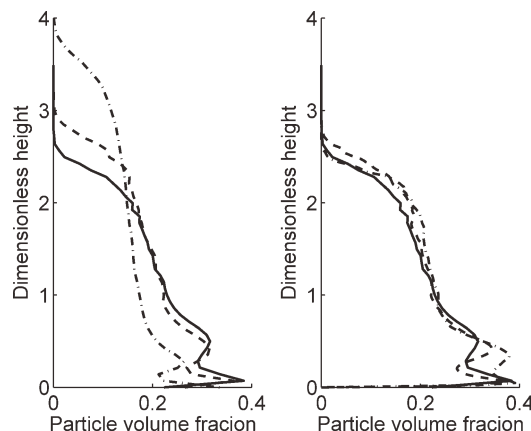

Figure 19. Vertical profiles of particle volume fraction.

Simulations results without and with the drag model are at the left and the right, respectively. —: $\Delta_G = 100\ \mu m$ (fully resolved simulation), ‑‑‑: $\Delta_G = 1$ mm, ‑‑‑‑: $\Delta_G = 2$ mm.

0.99. As seen in Figures 13 and 14, these events are very infrequent so they are expected to have a negligible effect.

Coarse-grid simulation of the reference case

The reference case defined in the "A Priori Analysis Description" section is used to validate the model. Simulations were performed on meshes of sizes 2 mm and 1 mm. A snapshot of the particle volume fraction obtained on the 2 mm-size mesh is shown in Figure 18. As shown in Figure 19, the correct bed expansion is well predicted with the two coarse meshes.

We define K_{yy}^{moy} the time average of K_{yy} by:

$$K_{yy}^{moy} = \frac{\int \frac{\overline{\alpha}_p \rho_p}{\overline{\tau}_p} \widetilde{W}_{r,y} f(\overline{\Delta}^*)\, h(\overline{\alpha}_p)\, K_{yy}\, dt}{\int \frac{\overline{\alpha}_p \rho_p}{\overline{\tau}_p} \widetilde{W}_{r,y} f(\overline{\Delta}^*)\, h(\overline{\alpha}_p)\, dt} \tag{43}$$

Vertical profiles of K_{yy}^{moy} for different the meshes are shown in Figure 20. Oscillations on profiles of K_{yy}^{moy} are due to the nonconvergence of the time average operation since
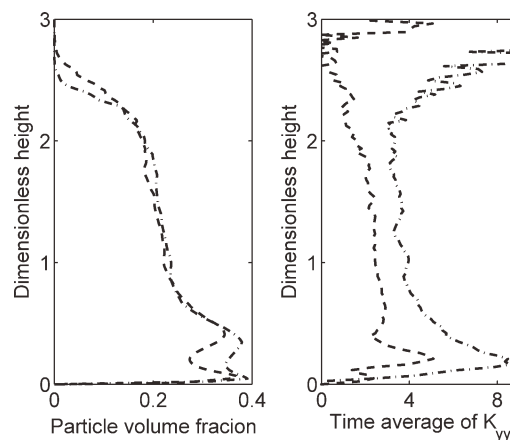

Figure 20. Vertical profiles of particle volume fraction and time average of K_{yy}, K_{yy}^{moy}.
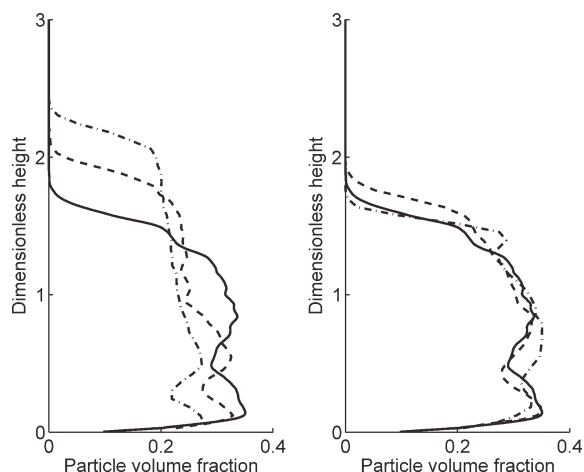
‑‑‑: $\Delta_G = 1$ mm, ‑‑‑‑: $\Delta_G = 2$ mm.

Figure 21. Vertical profiles of particle volume fraction in the larger bed.

Simulations results without and with the drag model are at the left and the right, respectively. —: $\Delta_G = 200\ \mu m$ (fully resolved simulation), ---: $\Delta_G = 2$ mm, -·-·: $\Delta_G = 4$ mm.

the particle volume fraction is very low. The theory developed assumes that K_{xx} is independent of the size of the mesh cells. However, its value changes slightly between the two coarse-grid simulations and this is probably due to errors in modelling f. Moreover, the value of K_{yy}^{moy} depends on the position within the bed.

Coarse-grid simulation of a larger bed

The same bed with a bed width of 0.06 m and a superficial velocity of 0.1 m/s was also simulated with and without the developed model. All the parameters of the model have been fixed to the same values used in the simulations of the reference case. Particularly, a was fixed to $6.13 \cdot 10^{-2}$ while its value was measured to $5.72 \cdot 10^{-2}$ in this case (see Table 3).

As shown in Figure 21, the correct bed expansion is well predicted with the two coarse meshes when the model is used while an overestimation is found without any models.

Coarse-grid simulation of Geldart B bubbling fluidized bed

While it has been shown that the model gives satisfactory results in the reference case, it should be also verified that the model vanishes when simulations without any model give satisfactory results. This fact is clearly not the case for scaling factor models.

A Geldart B fluidized bed with parameters extracted Makkawi et al.[12] experiments is simulated (*cf.*, Table 4). Coarse-grid simulations without any drag modification lead to good

Table 4. Physical Parameters of the Geldart B Fluidized Bed

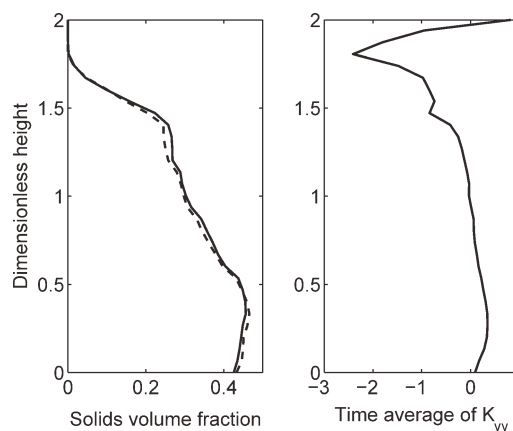|	
Bed width L	0.138 cm
Particle diameter d_p	350 μm
Particle density ρ_p	2500 kg/m^3
Restitution coefficient e_c	0.80
Gas density ρ_g	1.4 kg/m^3
Gas viscosity μ_g	1.8 10^{-5} Pa.s
Superficial gas velocity U_f	0.54 m/s

Figure 22. Vertical profiles of particle volume fraction and K_{yy}^{moy} for the Geldart B bubbling fluidized bed.

At left, —: without subgrid drag model, ---: with the subgrid drag model. At right, —: K_{yy}^{moy}.

agreement with experimental measurements of the bed expansion.[12,22] Therefore, we expect that no significant changes will appear when using the developed model. This is shown in Figure 22, where the results obtained on a mesh size of 9.86 mm are given. Consequently, it can be concluded that the model can be applied even if it is not needed.

The fact that coarse-grid simulations without any drag modification lead to good agreement with finest simulations is explained by the small values of the dimensionless number $\overline{\Delta}^*$ even when using coarse meshes. It is not an inherent property of group B particles, because disagreement is found when bed width is increased, has been shown by Wang et al.[34]

Extension to Three-Dimensional Cases

The results obtained previously were gathered in a two-dimensional case. Igci et al.[28] report that, although there are quantitative differences between the 2D and 3D results, they are qualitatively similar. We performed simulations of a bubbling fluidized bed in a 3D bed with a square section of 0.03 m width. Gas and particle characteristics were identical to
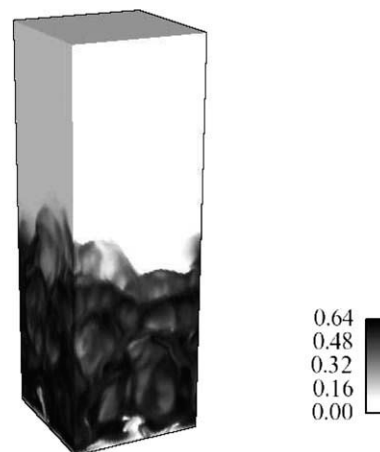

Figure 23. Snapshot of a the particle volume fraction field in the three-dimensional fluidized bed.
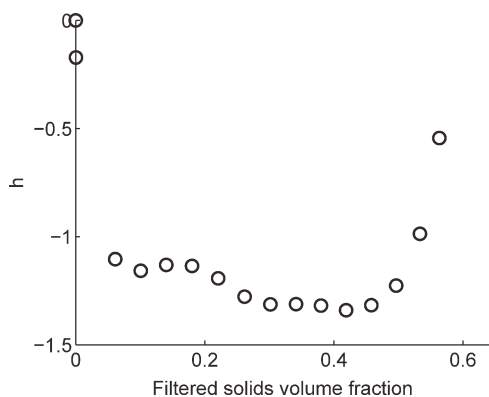
Figure 24. Measured values of as a function of the filtered particle volume fraction $\bar{\alpha}_p$ for the three-dimensional fluidized bed.

Filtering was performed using the box filter with $R = 15$.

the test case. The superficial gas velocity was 0.1 m/s. The initial bed height was 0.03 m with a particle volume fraction of 0.55. The domain height was 0.09 m. The cells of the mesh were cubes of 250 μm width, corresponding to $120 \times 120 \times 360 = 5{,}184{,}000$ cells. A snapshot of the particle volume fraction field is shown in Figure 23.

Correlative analysis indicates that the subgrid drift velocity can still be identified as Eq. 19. As seen in Figure 24, h is more independent of the filtered particle volume fraction than it is in the 2D case. However, the mesh is still too coarse to measure the function f correctly.

The test filter defined by Eq. 30 becomes, for three-dimensional cases:

$$\widehat{\overline{f}}(\mathbf{x}, t) = \frac{1}{7} \quad (\overline{f}(\mathbf{x}, t)$$
$$+ \overline{f}(\mathbf{x} + \Delta_G \mathbf{e_x}, t) + \overline{f}(\mathbf{x} - \Delta_G \mathbf{e_x}, t)$$
$$+ \overline{f}(\mathbf{x} + \Delta_G \mathbf{e_y}, t) + \overline{f}(\mathbf{x} - \Delta_G \mathbf{e_y}, t) \quad (44)$$
$$+ \overline{f}(\mathbf{x} + \Delta_G \mathbf{e_z}, t) + \overline{f}(\mathbf{x} - \Delta_G \mathbf{e_z}, t))$$

Then, $\widehat{\overline{\Delta}}$ is linked to $\overline{\Delta}$ by:

$$\widehat{\overline{\Delta}}^2 = \overline{\Delta}^2 + \frac{24}{7} \Delta_G^2 \quad (45)$$

For two-dimensional simulations in the (x, z) plane, K_{xx} and K_{yy} are calculated using Eq. 36. In three-dimensional simulations, where the gravity is in the z-direction, it is assumed that $K_{xx} = K_{yy}$. Then, following Lilly,[41] K_{xx} and K_{yy} are calculated by:

$$K_{xx} = K_{yy} = -\frac{L_x M_x + L_y M_y}{M_x^2 + M_y^2} \quad (46)$$

Conclusion and Perspectives

The filtered approach was used as a starting point to deal with the effect of unresolved structures on the resolved flow, during numerical simulations. Using highly resolved simulation, we have first-shown that the first order term that need to be modelled is the unresolved part of the filtered drag. Then, using a correlative analysis, we reduce the problem to the prediction of a subgrid drift velocity coming from spatial inhomogeneities inside the filtered volume and the correlation between gas phase and particle volume fraction. A mathematical analysis for small filter sizes as shown a square dependence of the subgrid drift velocity. The subgrid drift velocity was modelled as a function of the filtered particle volume fraction, the resolved relative velocity, and the filter size. The model is adjusted using a dynamic procedure adapted from single-phase turbulence modelling. Tests on coarse-grid simulations have shown a good prediction of the bed expansion for any mesh size. Finally, an extension to three-dimensional cases has been suggested.

One of our objective was to provide a generic model, with the minimum of adjustable parameters and that is easily implementable in a CFD code. While in the present form the model seems limited to bubbling fluidized beds, the methodology used to develop it is not specific of this case. Future work will be to extend the results to other flow configurations, such as circulating fluidized beds. In these cases, where the particle volume fraction is lower than in dense beds, the subgrid scales can play a major role on the particle agitation and new closure terms have to be derived.

Literature Cited

1. Kunii D, Levenspiel O. *Fluidization Engineering*. Boston: Butterworth- Heinemann, 1991.
2. Van der Hoef MA, Ye M, van Sint Annaland M, Andrews AT, Sundaresan S, Kuipers JAM. Multiscale modeling of gas-fluidized beds. *Adv Chem Eng*. 2006;31:66.
3. Van der Hoef MA, van Sint Annaland M, Deen NG, Kuipers JAM. Numerical simulation of dense gas-solid fluidized beds: a multiscale modeling strategy. *Annu Rev Fluid mech*. 2008;40:47–70.
4. Balzer G, Boelle A, Simonin O. Eulerian gas-solid flow modelling of dense fluidized bed. *Fluidization*. 1995;8:1125.
5. Ding J, Gidaspow D. A bubbling fluidization model using kinetic theory of granular flow. *AIChE J*. 1990;36:523–538.
6. Gobin A, Neau H, Simonin O, Llinas J, Reiling V, Slo J. Fluid dynamic numerical simulation of a gas phase polymerisation reactor. *Int J Numer Meth Fluids*. 2003;43:1199–1220.
7. Peirano E, Delloume V, Leckner B. Two- or three-dimensional simulations of turbulent gas–solid flows applied to fluidization. *Chem Eng Sci*. 2001;56:4787–4799.
8. Van Wachem BGM, Schouten JC, Van den Bleek CM, Krishna R, Sinclair JL. Comparative analysis of CFD models of dense gas–solid systems. *AIChE J*. 2001;47:1035–1051.
9. Ferschneider G, Mege P. Eulerian simulation of dense phase fluidized beds. *Oil Gas Sci Technol*. 1996;51:301–307.
10. Gao J, Lan X, Fan Y, Chang J, Wang G, Lu C, Xu C. CFD modeling and validation of the turbulent fluidized bed of FCC particles. *AIChE J*. 2009;55:1680–1694.
11. Hosseini SH, Rahimi R, Zivdar M, Samimi A. CFD simulation of gas-solid bubbling fluidized bed containing FCC particles. *Kor J Chem Eng*. 2009;26:1405–1413.
12. Makkawi YT, Wright PC, Ocone R. The effect of friction and interparticle cohesive forces on the hydrodynamics of gas–solid flow: a comparative analysis of theoretical predictions and experiments. *Powder Technol*. 2006;163:69–79.

13. McKeen T, Pugsley T. Simulation and experimental validation of a freely bubbling bed of FCC catalyst. *Powder Technol*. 2003;129:139–152.
14. Wang J. A review of eulerian simulation of geldart a particles in gas-fluidized beds. *Ind Eng Chem Res*. 2009;48:5567–5577.
15. Zimmermann S, Taghipour F. CFD modeling of the hydrodynamics and reaction kinetics of FCC fluidized-bed reactors. *Ind Eng Chem Res*. 2005;44:9818–9827.
16. Ergun S. Fluid flow through packed columns. *Chem Eng Prog*. 1952;48:89–94.
17. Gibilaro LG, Di Felice R, Waldram SP, Foscolo PU. Generalized friction factor and drag coefficient correlations for fluid-particle interactions. *Chem Eng Sci*. 1985;40:1817–1823.
18. Gidaspow D. *Multiphase flow and fluidization: continuum and kinetic theory descriptions*. Boston: Academic Press, 1994.
19. Van der Hoef MA, Beetstra R, Kuipers JAM. Lattice-Boltzmann simulations of low-Reynolds-number flow past mono-and bidisperse arrays of spheres: results for the permeability and drag force. *J Fluid Mech*. 2005;528:233–254.
20. Syamlal M, O'Brien TJ. Computer Simulation of Bubbles in a Fluidized Bed, in Fluidization and Fluid Particle Systems: Fundamentals and Applications, Ed. L.-S. Fan, AIChE Symposium Series No, 270, 85, 1989;22–31.
21. Wen CY, Yu YH. Mechanics of fluidization. In: *Chem. Eng. Prog. Symp. Ser*, vol. 62, 1966:100–111.
22. Circulating Fluidized Bed Technology IX. Werther J, Nowak W, Wirth K-E, Hartge E-U, editors. Proceedings of the 9th international Conference on Circulating Fluidized Beds, May 13–16, 2008, Hamburg, Germany.
23. Wang J, Van der Hoef MA, Kuipers JAM. Why the two-fluid model fails to predict the bed expansion characteristics of Geldart A particles in gas-fluidized beds: a tentative answer. *Chem Eng Sc*. 2009;64:622–625.
24. Gidaspow D, Bezburuah R, Ding J. Hydrodynamics of circulating fluidized beds: kinetic theory approach. In: *Fluidization VII: proceedings of the Seventh Engineering Foundation Conference on Fluidization, May 3–8, 1992, Brisbane, Australia*. Amer Inst of Chemical Engineers, 1992: 75.
25. Agrawal K, Loezos PN, Syamlal M, Sundaresan S. The role of meso-scale structures in rapid gas–solid flows. *J Fluid Mech*. 2001; 445:151–185.
26. Andrews IV AT, Loezos PN, Sundaresan S. Coarse-grid simulation of gas-particle flows in vertical risers. *Ind Eng Chem Res*. 2005;44: 6022–6037.
27. Heynderickx GJ, Das AK, De Wilde J, Marin GB. Effect of clustering on gas-solid drag in dilute two-phase flow. *Ind Eng Chem Res*. 2004;43:4635–4646.
28. Igci Y, Andrews AT IV, Sundaresan S, Pannala S, O'Brien T. Filtered two-fluid models for fluidized gas-particle suspensions. *AIChE J*. 2008;54:1431–1448.
29. Zhang DZ, VanderHeyden WB. The effects of mesoscale structures on the macroscopic momentum equations for two-phase flows. *Int J Multiphase Flow*. 2002;28:805–822.
30. Wang J, Liu Y. Emms-based eulerian simulation on the hydrodynamics of a bubbling fluidized bed with fcc particles. *Powder Technol*. 2010;197:241–246. doi:DOI: 10.1016/j.powtec.2009.09.022.
31. Li J, Kwauk M. *Particle-Fluid Two-Phase Flow: the Energy-Minimization Multi-Scale Method*. Beijing, P.R. China.: Metallurgical Industry Press, 1994.
32. Wang W, Li JH. Simulation of gas-solid two-phase flow by a multiscale CFD approach-Extension of the EMMS model to the sub-grid level. *Chem Eng Sci*. 2007;62:208–231.
33. Wang J, Ge W, Li J. Eulerian simulation of heterogeneous gas-solid flows in CFB risers: EMMS-based sub-grid scale model with a revised cluster description. *Chem Eng Sci*. 2008;63:1553–1571.
34. Wang J, van der Hoef MA, Kuipers JAM. Coarse grid simulation of bed expansion characteristics of industrial-scale gas-solid bubbling fluidized beds. *Chem Eng Sci*. 2010;65:2125–2131. doi:DOI: 10.1016/j.ces.2009.12.004.
35. Richardson JF, Zaki WN. Sedimentation and fluidisation: part I. *Chem Eng Res Des*. 1954;32:35–53.
36. Smagorinsky J. General circulation experiments with the primitive equations. *Monthly Weather Rev*. 1963;91:99–164.
37. Guelfi A, Bestion D, Boucker M, Boudier P, PILLION P, Grandotto M, Herard J, Hervieu E, Peturaud P. NEPTUNE: a new software platform for advanced nuclear thermal hydraulics. *Nuclear Sci Eng*. 2007;156:281–324.
38. De Wilde J. Reformulating and quantifying the generalized added mass in filtered gas-solid flow models. *Phys Fluids*. 2005;17:113304.
39. De Wilde J. The generalized added mass revised. *Phys Fluids*. 2007;19:058103.
40. Germano M, Piomelli U, Moin P, Cabot WH. A dynamic subgrid-scale eddy viscosity model. *Phys Fluids A: Fluid Dyn*. 1991;3:1760.
41. Lilly DK. A proposed modification of the Germano subgrid-scale closure method. *Phys Fluids A: Fluid Dyn*. 1992;4:633.
42. Boelle A, Balzer G, Simonin O. Second-order prediction of the particle-phase stress tensor of inelastic spheres in simple shear dense suspensions. In: *Gas-Particle Flows*, vol. 228. ASME FED; 1995:9–18.
43. Lun CKK, Savage SB. The effects of an impact velocity dependent coefficient of restitution on stresses developed by sheared granular materials. *Acta Mechanica*. 1986;63:15–44.
44. Clark RA, Ferziger JH, Reynolds WC. Evaluation of subgrid-scale models using an accurately simulated turbulent flow. *J Fluid Mech*. 1979;91:1–16.

Appendix

Two-fluid model equations

The model is based on separate equations of mass and momentum for the gas phase and on mass, momentum, and kinetic agitation for the particle phase. Equations are coupled through gas and particle volume fraction and inter-phase momentum transfer terms. In the following, subscript $k = g$ refers to the gas phase and $k = p$ to the particle phase. The following equations were derived by Refs. 4 and 42.

Gas and particle volume fraction, α_g and α_p have to satisfy:

$$\alpha_g + \alpha_p = 1 \tag{A1}$$

Mass transport equation:

$$\frac{\partial}{\partial t}(\alpha_k \rho_k) + \frac{\partial}{\partial x_i}(\alpha_k \rho_k U_{k,i}) = 0 \tag{A2}$$

with ρ_k density of the k phase and $U_{k,i}$ the i-component of its velocity.

Momentum transport equation:

$$\alpha_k \rho_k \left(\frac{\partial U_{k,i}}{\partial t} + U_{k,j} \frac{\partial U_{k,i}}{\partial x_j} \right) = -\alpha_k \frac{\partial P_g}{\partial x_i} + \alpha_k \rho_k g_i \\ + I_{k,i} + \frac{\partial}{\partial x_j} \Sigma_{k,ij} \tag{A3}$$

with P_g the mean gas pressure, g_i the gravity i-component, $I_{k,i}$ the inter-phase momentum transfer without the mean gas pressure contribution, $I_{g,i} = -I_{p,i}$, and $\Sigma_{k,ij}$ the effective stress tensor of the phase k. For $k = g$, it is equal to the laminar viscous stress tensor. The stress tensor for the particular phase is closed using a Boussinesq hypothesis:

$$\Sigma_{p,ij} = \left(P_p - \lambda_p \frac{\partial U_{p,m}}{\partial x_m} \right) \delta_{ij} \\ - \mu_p \left(\frac{\partial U_{p,i}}{\partial x_j} + \frac{\partial U_{p,j}}{\partial x_i} - \frac{2}{3} \frac{\partial U_{p,m}}{\partial x_m} \delta_{ij} \right) \tag{A4}$$

with P_p the particular pressure, $\mu_p = \alpha_p \rho_p (v_p^{kin} + v_p^{coll})$ the shear particular viscosity and λ_p the volume particular viscosity. P_p, v_p^{kin}, v_p^{coll} and λ_p are given by:

$$P_p = \frac{2}{3}\alpha_p \rho_p \, q_p^2 \, (1 + 2\alpha_p g_0 \, (1 + e_c)) \tag{A5}$$

$$\lambda_p = \frac{4}{3}\alpha_p \rho_p \alpha_p g_0 \, d_p \, (1 + e_c)\sqrt{\frac{2 q_p^2}{3\pi}} \tag{A6}$$

$$v_p^{kin} = \frac{1}{3}\tau_p \, q_p^2 \, (1 + \alpha_p g_0 \, \phi_c)\left(1 + \frac{\sigma_c}{2}\frac{\tau_p}{\tau_c}\right)^{-1} \tag{A7}$$

$$v_p^{coll} = \frac{4}{5}\alpha_p g_0 (1 + e_c)\left(v_p^{kin} + d_p\sqrt{\frac{2 q_p^2}{3 \, \pi}}\right) \tag{A8}$$

with e_c particles elasticity coefficient, $\sigma_c = (1 + e_c)(3 - e_c)/5$ and $\phi_c = 2/5 \, (1 + e_c)(3e_c - 1)$. τ_p is the particle relaxation time given by the drag law. The inter-particle collisions time τ_c is given by:

$$\frac{1}{\tau_c} = 24 \, \frac{\alpha_p g_0}{d_p}\sqrt{\frac{2 q_p^2}{3 \, \pi}} \tag{A9}$$

The pair correlation function g_0 reflects the increase of the probability to find a particle at contact due to the close packing of particles. Lun and Savage[43] give the following expression:

$$g_0 = \left(1 - \frac{\alpha_p}{\alpha_m}\right)^{-2.5\alpha_m} \tag{A10}$$

which tends to infinity when the particle volume fraction α_p tends to $\alpha_m = 0.64$, the maximum solid fraction. The particle random kinetic energy q_p^2- or so-called "granular temperature" obeys the following transport equation, which is derived from the particle pdf Boltzman-like equation:

$$\alpha_p \rho_p \left(\frac{\partial q_p^2}{\partial t} + U_{k,j}\frac{\partial q_p^2}{\partial x_j}\right) = \frac{\partial}{\partial x_j}\left(\alpha_p \rho_p (K_p^{kin} + K_p^{coll})\frac{\partial q_p^2}{\partial x_i}\right)$$
$$-\Sigma_{p,ij}\frac{\partial U_{p,j}}{\partial x_i} - 2\,\frac{\alpha_p \rho_p}{\tau_p}q_p^2 - \frac{1}{2}(1 - e_c^2)\frac{\alpha_p \rho_p}{\tau_c}\frac{2}{3}q_p^2 \tag{A11}$$

with K_p^{kin} and K_p^{coll} the kinematic and collisional diffusivity respectively, given by:

$$K_p^{kin} = \frac{2}{3}\,q_p^2 \tau_c (1 + \alpha_p g_0 \varphi_c)\left(\xi_c + \frac{9}{5}\frac{\tau_c}{\tau_p}\right)^{-1} \tag{A12}$$

$$K_p^{coll} = \frac{6}{5}\alpha_p g_0 \, (1 + e_c)\left(K_p^{kin} + \frac{10}{9}d_p\sqrt{\frac{2 q_p^2}{3 \, \pi}}\right) \tag{A13}$$

with $\xi_c = (1 + e_c)(49 - 33e_c)/100$ and $\varphi_c = 3/5(1 + e_c)^2(2e_c - 1)$. The interface momentum transfer, $I_{k,i}$, can be written as:

$$I_{p,i} = -\frac{\alpha_p \rho_p}{\tau_p}(U_{p,i} - U_{g,i}) \tag{A14}$$

with τ_p the particle relaxation time given by the Wen and Yu[21] correlation:

$$\frac{1}{\tau_p} = \frac{1}{\tau_p^{St}}\left(1 + 0.15R_e^{0.687}\right)\alpha_g^{-2.7} \tag{A15}$$

with $R_e = \alpha_g\|\mathbf{U_p} - \mathbf{U_g}\|d_p/v_g$ and $\tau_p^{St} = \rho_p d_p^2/(18\mu_g)$ the Stokes drag time of an isolated spherical particle in the gas.

Taylor development for the subgrid drift velocity

Using Taylor expansions, a mathematical expression of the subgrid drift velocity can be written in function of gradient of the filtered values. This method is adapted from works on LES in single phase flows.[44] Let us consider a variable f, which is a function of space and time. A Taylor series expansion of f around $\mathbf{x_0}$ leads to:

$$f(\mathbf{x}) \simeq f(\mathbf{x_0}) + \left.\frac{\partial f}{\partial x_i}\right|_{\mathbf{x_0}}(x_i - x_{0,i})$$
$$+ \frac{1}{2}\left.\frac{\partial^2 f}{\partial x_i \partial x_j}\right|_{\mathbf{x_0}}(x_i - x_{0,i})(x_j - x_{0,j}) + \ldots \tag{A16}$$

Multiplying this expansion by $G(\mathbf{x_0} - \mathbf{x})$ and integrating $\mathbf{x}$ over the whole space leads to:

$$\bar{f} \simeq f + \frac{\partial f}{\partial x_i}\bar{I}_i + \frac{1}{2}\frac{\partial^2 f}{\partial x_i \partial x_j}\bar{I}_{ij} + \ldots \tag{A17}$$

were $\bar{I}_i$ and $\bar{I}_{i,j}$ are defined as follows:

$$\bar{I}_i = \iiint G(\mathbf{u})u_i\,\mathbf{du} \tag{A18}$$

$$\bar{I}_{ij} = \iiint G(\mathbf{u})u_i u_j\,\mathbf{du} \tag{A19}$$

Assuming that the kernel G is an even function, we obtained $\bar{I}_i = 0$ and $\bar{I}_{i,j\neq i} = 0$. Multiplying Eq. A16 by $G(\mathbf{x_0} - \mathbf{x})$ $\alpha_k(\mathbf{x})$ and integrating $\mathbf{x}$ over the whole space leads to:

$$\overline{\alpha_k f} \simeq \overline{\alpha_k}f + \frac{\partial f}{\partial x_i}\,\bar{\alpha}_k \widetilde{I}_i^k + \frac{1}{2}\frac{\partial^2 f}{\partial x_i \partial x_j}\,\bar{\alpha}_k \widetilde{I}_{ij}^k + \ldots \tag{A20}$$

were $\widetilde{I}_i^k$ and $\widetilde{I}_{i,j}^k$ are defined as follows:

$$\widetilde{I}_i^k = \frac{1}{\bar{\alpha}_k}\iiint G(\mathbf{u}) \, u_i \, \alpha_k(\mathbf{x_0} + \mathbf{u}) \, \mathbf{du} \tag{A21}$$

$$\widetilde{I}_{ij}^k = \frac{1}{\bar{\alpha}_k}\iiint G(\mathbf{u}) \, u_i u_j \, \alpha_k(\mathbf{x_0} + \mathbf{u}) \, \mathbf{du} \tag{A22}$$

Performing a Taylor series expansion of α_k around $\mathbf{x_0}$ and putting it in Eqs. A21 and A22 leads to:

$$\widetilde{I}_i^k \simeq \frac{1}{\overline{\alpha}_k} \frac{\partial \alpha_k}{\partial x_j} \, \overline{I}_{ij} \; + \; \dots \tag{A23}$$

$$\widetilde{I}_{ij}^k \simeq \frac{\alpha_k}{\overline{\alpha}_k} \, \overline{I}_{ij} + \dots \tag{A24}$$

Now using Eqs. A17, A20, A23, and A24 for both α_p, α_g, and $U_{g,i}$ leads to the following expressions for $\widetilde{U}_{g,i}$ and $\widetilde{U}_{g@p,i}$:

$$\widetilde{U}_{g,i} \simeq U_{g,i} + \frac{1}{\overline{\alpha}_g} \frac{\partial \alpha_g}{\partial x_j} \frac{\partial U_{g,i}}{\partial x_j} \, \overline{I}_{jj} + \frac{1}{2} \frac{\partial^2 U_{g,i}}{\partial x_j \partial x_j} \, \overline{I}_{jj} + \dots \tag{A25}$$

$$\widetilde{U}_{g@p,i} \simeq U_{g,i} + \frac{1}{\overline{\alpha}_p} \frac{\partial \alpha_p}{\partial x_j} \frac{\partial U_{g,i}}{\partial x_j} \overline{I}_{jj} + \frac{1}{2} \frac{\partial^2 U_{g,i}}{\partial x_j \partial x_j} \overline{I}_{jj} + \dots \tag{A26}$$

Then subtracting Eq. A25 from Eq. A26 leads to the following expression for the drift velocity:

$$\overline{\alpha}_p \, \overline{\alpha}_g \widetilde{V}_{d,i} = \frac{\overline{\Delta}^2}{12} \frac{\partial \alpha_p}{\partial x_j} \frac{\partial U_{g,i}}{\partial x_j} + O(\overline{\Delta}^4) \tag{A27}$$

where the characteristic length scale $\overline{\Delta}$ is defined by:

$$\overline{\Delta}^2 = 12 \, I_{11} = 12 \, I_{22} = 12 \, I_{33} \tag{A28}$$

In the case of the continuous box or top-hat filter defined as follows:

$$G(\mathbf{u}) = \begin{cases} 1/\Delta_B^3 & \text{if } max(u_x, u_y, u_z) < \Delta_B/2 \\ 0 & \text{otherwise} \end{cases} \tag{A29}$$

we have:

$$\overline{I}_{11} = \overline{I}_{22} = \overline{I}_{33} = \frac{1}{12} \Delta_B^2 = \frac{1}{12} \overline{\Delta}^2 \tag{A30}$$

In the case of the spectral cut-off filter, Eq. A17 and so on model Eq. A27 are not valid since $\overline{I}_{11} = \overline{I}_{22} = \overline{I}_{33} = \infty$. In the case of the discrete version of the box filter, as defined in the "A Priori Analysis Description" section, we have:

$$\overline{\Delta}^2 = \Delta_B^2 \left(1 - \left(\frac{\Delta_D}{\Delta_B} \right)^2 \right) \tag{A31}$$